Journal of Materials Chemistry A



PAPER

View Article Online
View Journal | View Issue



Cite this: J. Mater. Chem. A, 2024, 12, 17229

Harnessing the power of thermoplastic elastomerderived ordered mesoporous carbons through functionalization†

Mark Robertson,^a Andrew Barbour,^a Anthony Griffin, ^{ba} Jeffrey Aguinaga,^a Derek Patton, ^{ba} Yizhi Xiang ^{ba} and Zhe Qiang ^{ba}

Ordered mesoporous carbons (OMCs) have shown great promise in a variety of applications, including adsorption, energy storage, and catalysis. To elevate their performance further, it is important to introduce additional functionalities into their composition and surface chemistry, as well as to enhance their pore surface area. Recently, a simple method for OMC synthesis is established through leveraging commodity thermoplastic elastomers (TPEs) as precursors. In this system, a sulfonation-induced crosslinking reaction is employed to selectively crosslink the olefinic majority phase of TPEs, enabling its conversion to carbon upon pyrolysis, while decomposing the styrenic minority phase to develop mesopores. Building on this platform approach, this works demonstrates multiple functionalization pathways to modulate pore texture and chemical composition of TPE-derived OMCs, which can allow their further and enhanced use in a variety of applications. This work first shows that chemical activation can significantly enhance the surface area of TPE-derived OMCs, increasing from 485 m² g⁻¹ to approximately 1250 m² q⁻¹. Furthermore, the introduction of dopants into crosslinked TPEs facilitates the incorporation of heteroatoms, such as boron, nitrogen, sulfur, and phosphorus into the carbon framework during carbonization. The hydrophilic nature of the crosslinked polymer also enables the incorporation of water-soluble metal nitrates, which can then form metal nanoparticles within the carbon framework upon carbonization. Collectively, this work demonstrates simple and scalable methods to improve the capabilities of TPE-derived OMCs via functionalization, including chemical activation to increase surface area, heteroatom doping, and introducing nanoparticles into the carbon framework.

Received 16th April 2024 Accepted 14th June 2024

DOI: 10.1039/d4ta02629b

rsc.li/materials-a

Introduction

Nanoporous carbons are ubiquitous for various applications, such as water remediation, ^{1,2} catalysis, ³⁻⁵ biomedicine, ^{6,7} and energy storage. ⁸⁻¹⁰ Their porous nature can allow the sorption, storage, and transport of guest molecules, while the carbon framework provides advantages of chemical inertness and performance stability. While activated carbons have been broadly used in large-scale, commercial applications due to

their high surface area, their small and disordered pores (pore size < 2 nm) may limit the ability to address relatively large-sized guest molecules, such as proteins and per-/polyfluoroalkyl substances (PFAS). 11,12 Alternatively, ordered mesoporous carbons (OMCs), containing uniform pores with sizes ranging from 2 to 50 nm, can promote mass transport and diffusion of various species into the carbon matrix, while maintaining relatively high surface areas, 13-15 leading to enhanced performance in many applications compared to their microporous counterparts.

Conventionally, OMCs can be prepared by a soft-templating method or direct pyrolysis of block copolymer precursors; both approaches involve a self-assembly process, followed by cross-linking and carbonization steps. 8,16-19 To further enhance the utility and performance of OMCs, many research efforts have been focused on developing functionalization methods, which can alter the physical or chemical characteristics of OMCs, such as pore texture, surface functionality, as well as material composition. 20-22 For instance, a common method for increasing surface area of OMCs is through chemical activation, which can partially etch out the carbon matrix to form

[&]quot;School of Polymer Science and Engineering, University of Southern Mississippi, 39406, Hattiesburg, Mississippi, USA. E-mail: zhe.qiang@usm.edu

^bDave C. Swalm School of Chemical Engineering, Mississippi State University, Mississippi State, 39762, Mississippi, USA

[†] Electronic supplementary information (ESI) available: Supporting information including SAXS patterns, physisorption isotherms, NLDFT pore size distributions, and SEM images of SEBS-derived OMCs, activated OMCs, heteroatom doped OMCs, and metal nanoparticle-loaded OMCs are all provided. In addition, XPS results for the SEBS-derived OMCs after various functionalization methods, and domain spacings derived from SAXS patterns for the metal loaded samples are available. See DOI: https://doi.org/10.1039/d4ta02629b

micropores. Chemical agents that have been used for carbon activation include potassium hydroxide (KOH), steam, CO2, and inorganic salts.23 Lv et al. demonstrated that activation of softtemplated OMCs can greatly enhance their performance in supercapacitors by elevating the OMC surface area from 660 m² g⁻¹ to 1410 m² g⁻¹.²⁴ Additionally, heteroatoms (including nitrogen, sulfur, boron, and phosphorus) can be incorporated into the carbon framework of OMCs through various methods, including using heteroatom-containing carbon precursors, coassembly of dopants with carbon precursors, and in situ incorporation of heteroatoms during the formation of the carbonaceous species.25,26 The introduction of heteroatoms leads to altered functionality of pore surface, potentially allowing more favored interactions between the carbon matrix and specific molecules of interest to increase OMC utility. 27,28 As an example, Liu et al. synthesized boron-doped OMCs through a hardtemplating method by mixing boric acid with sucrose.29 After carbonization, approximately 1 at% of boron was incorporated into the carbon material, resulting in a ~40% increase in maximum adsorption capacity of Pb(II) ions of the OMCs.

Moreover, the incorporation of metal nanoparticles into OMCs can also lead to enhanced performance for water remediation and energy storage.30-32 This can be accomplished through various methods, including but not limited to, anchoring nanoparticles into carbon framework, as well as the cooperative self-assembly of polymeric templates, carbon precursors, and metal nanoparticle precursors.33,34 Kou et al. synthesized nitrogen-doped, hierarchically porous carbons using silica colloidal crystals as a macroporous scaffold and poly(ethylene oxide)-block-poly(propylene oxide)-block-poly(ethylene oxide) (PEO-b-PPO-b-PEO) as a template for developing mesopores, with the inclusion of dicyandiamide and nickel nitrate hexahydrate as nitrogen dopants and metal nanoparticle precursors, respectively.35 From the incorporation of nickel nanoparticles through this method, the faradaic efficiency of the OMCs increases by up to 70% in electrocatalytic reduction of CO₂ in comparison to the analogous with the absence of metal species. From these literature precedents, it is apparent that functionalization processes can enable the improved performance of OMCs to address various application needs. However, the synthesis of functionalized OMCs can often be intricate, involving multiple steps, and/or expensive chemical agents. There is a need to develop simple and scalable approaches for unlocking the transformative potential of OMCs, particularly for practical applications that require largescale production.

Recent works have demonstrated a cost-effective strategy for fabricating OMCs using styrenic thermoplastic elastomers (TPE) as precursors, in conjunction with sulfonation-induced crosslinking chemistry.^{36–38} Specifically, the sulfonation-induced crosslinking reaction selectively crosslinks the polyolefin majority phase of triblock copolymer TPEs, enabling them to become efficient carbon precursors. Upon pyrolysis, the minority PS phase that does not undergo crosslinking is thermally decomposed while the crosslinked olefinic majority phase is converted to carbon, resulting in the formation of OMC. While these works demonstrate the fundamental processes of

OMC synthesis with key advantages of low cost and simple process, they primarily focused on precursor design and process optimization; expanding the material and system design space to enhance their functionalities has not been explored. Addressing this technology gap in TPE-derived OMCs can provide an efficient pathway for further broadening their applications with improved performance across energy storage, water remediation, heterogenous catalysis, among many others.

Here, this work demonstrates a versatile platform for functionalizing TPE-derived OMCs, enabling their enhanced surface areas, and the incorporation of metal nanoparticles and heteroatoms into the carbon frameworks. Specifically, after the sulfonation-induced crosslinking step, the precursor becomes hydrophilic due to the installation of sulfonic acid functional groups on the polymer backbone. This hydrophilicity nature is leveraged to introduce water-soluble metal nitrates into the crosslinked polymers, which allows the formation of nanoparticles during the pyrolysis step. Additionally, the crosslinked material can be blended with various dopants for doping OMC framework. During the pyrolysis step, heteroatoms can be incorporated into the carbon framework *in situ*. Moreover, TPE-derived OMCs can be chemically activated through exposure to KOH at 700 °C, leading to elevated surface areas.

Experimental

Materials

Polystyrene-*block*-poly(ethylene-*ran*-butylene)-*block*-polystyrene (SEBS) ($M_{\rm n}=66\,000~{\rm g~mol^{-1}}$, D=1.08, $\phi_{\rm PS}=0.18$), calcium nitrate tetrahydrate (>99.0%), boric anhydride (99.98%), melamine (99%), and ammonium dihydrogen phosphate (99.999%) were purchased from Sigma-Aldrich. Copper nitrate hemipentahydrate (98%) and sodium hydroxide (97%) were purchased from Fisher Scientific, dibenzyl disulfide was obtained from TCI Chemicals, and both nickel nitrate hexahydrate (98%) and potassium hydroxide (97.0%) were purchased from Alfa Aesar. All compounds were used as received without further purification. Deionized (DI) water was obtained by passing tap water through a Millipore Mill-Q Type 1 filtration system.

Sulfonation-induced crosslinking SEBS and carbonization

In a typical crosslinking reaction, 300 mg of SEBS and 3 g of sulfuric acid were introduced into a 100 mL round bottom flask with a stir bar. The flask was placed into a bath of thermal beads that was preheated to 150 °C and the flask was heated for 4 h. After reaction, the polymer was removed from the acid by passing the mixture through a glass fritted funnel. To remove residual acid, the polymer was washed with 200 mL of DI water at least 3 times, and then dried under vacuum at 40 °C for 12 h before further use. The dried, crosslinked SEBS material was pyrolyzed at 800 °C in a tube furnace (MTI Corporation, OTF-1200X) under nitrogen atmosphere using the following heating schedule: the sample was heated from room temperature to 600 °C at a ramp rate of 1 °C min⁻¹ and then to 800 °C at a ramp rate of 5 °C min⁻¹.

Activation of OMCs

Chemical activation was carried out by first physically blending OMCs with potassium hydroxide (KOH) at various KOH: OMC mass ratios, including 1:1,1:2,1:3, and 1:4. This process was carried out by simply grinding the two materials using a mortar and pestle until a homogeneous mixture was formed. The mixture was then placed into a tube furnace and heated to 700 $^{\circ}$ C at a ramp rate of 10 °C min⁻¹ and held at 700 °C for 3 h for the activation to take place. After cooling, the mixture was washed 3 times with DI water to remove any residual byproducts from the reaction and separated from the aqueous solution through centrifugation. The resulting material was dried under vacuum at 40 °C for 12 h prior to characterization and further use.

Synthesis of heteroatom-doped OMCs

To dope heteroatoms into the OMCs, the sulfonated SEBS precursor was physically blended with boric anhydride (boron dopant), melamine (nitrogen dopant), ammonium dihydrogen phosphate (phosphorus dopant), or dibenzyl disulfide (sulfur dopant) at 1:1 mass ratio, respectively. The blending step was also carried out through grinding the mixtures with a mortar and pestle until a homogeneous mixture was formed. The mixture was then carbonized using the same procedure for converting crosslinked SEBS into doped-OMCs. After carbonization, the mixture was washed with 6 M NaOH solution for 72 h, where the solution was refreshed every 24 h, to remove any residual byproducts from the doping reactions. The doped OMCs were then washed with DI water to remove residual NaOH and separated from the liquid phase through centrifugation. Finally, the samples were dried under vacuum at 40 °C for 12 h.

Incorporation of metal nanoparticles into SEBS-derived OMCs

Metal nitrate solutions were prepared by dissolving different metal nitrates (including calcium nitrate tetrahydrate, copper nitrate hemipentahydrate, and nickel nitrate hexahydrate) in DI water, at concentrations ranging from 0.1 wt% to 1 wt%. Metal nitrates were then introduced into the crosslinked SEBS precursor by soaking 100 mg of SEBS in 10 mL of metal nitrate solution for 24 h. The precursor was then removed from the solution and dried under vacuum. After drying, the metal nitrate containing SEBS precursor was heated to 800 °C in a tube furnace under a nitrogen atmosphere. The carbonization procedure used is described as follows: the samples were heated from room temperature to 600 °C by increasing temperature at a rate of 1 °C min⁻¹, followed by increasing the temperature to 800 °C at a rate of 5 °C min⁻¹. After reaching 800 °C, the samples were held at this temperature for 3 h before allowing them to ambiently cool down to room temperature.

Characterization

Fourier transform infrared (FTIR) spectroscopy was performed using 32 scans at a resolution of 1 cm⁻¹ with a Nicolet 6700 spectrometer from Thermo Fisher. Water contact angle measurements were taken using a goniometer from Ramé-hart

Instrument Co. 10 µL droplets were used and the resulting images were analyzed with DROPimage software. A Zeiss Ultra 60 field-emission scanning electron microscope (SEM) was used to record high resolution images of the OMC pore texture by employing an accelerating voltage of 17 kV. Nitrogen physisorption experiments were carried out using a Tristar II from Micromeritics. The Brunauer-Emmett-Teller (BET) method was used to calculate the surface area, and the pore size distribution was determined from the adsorption branch of the physisorption isotherms using non-local density functional theory (NLDFT). Small angle X-ray scattering (SAXS) experiments were performed at the National Synchrotron Light Source II within Brookhaven National Laboratory. The experiments were performed at beamline 11-BM with a sample-to-detector distance of 5.05 m and an X-ray energy of 12 keV. The 2-dimensional scattering patterns were reduced into 1-dimensional results using packages developed in-house at the beamline of 11-BM. All domain spacings were calculated using the equation of d = $2\pi/q$. An ESCALAB Xi+ spectrometer from Thermo Fisher was used to perform X-ray photoelectron spectroscopy experiments. The spectrometer was equipped with a monochromatic Al Ka Xray source (1486.6 eV, 400 μm spot size). Spectra were obtained using the standard magnetic lens mode and charge compensation at a base pressure of 3×10^{-7} mbar with a take of angle of 90°. Additionally, all high-resolution XPS scans were fitted using Avantage software from Thermo Fisher. Transmission electron microscopy (TEM) images were captured using a 2100TEM from JEOL operating at 200 kV. X-ray diffraction (XRD) experiments were performed using a Rigaku Ultima III XRD system with Cu K α radiation at a 2θ range of 10° – 80° with a wavelength of 1.54 Å.

Results and discussion

Converting thermoplastic elastomers (TPEs) to functionalized OMCs begins with the first step of sulfonation-induced crosslinking. Initially, a polystyrene-block-poly(ethylene-ranbutylene)-block-polystyrene (SEBS) precursor is reacted in concentrated sulfuric acid at 150 °C for 4 h in the solid state. As shown in Fig. 1(A), this reaction selectively crosslinks the polyolefin majority phase, while polystyrene (PS) in the minority phase undergoes sulfonation without any evidence of crosslinking. Specifically, sulfonic acid groups are first introduced to the olefinic poly(ethylene-ran-butylene) (PEB) backbone, which can then dissociate to form double bonds.39-41 Through further reactions, the double bonds can undergo radical initiation and form intermolecular crosslinks with other polymer chains. The sulfonation of PS at early stages of the reaction, followed by the sulfonation of the olefinic majority phase, result in a significantly swelled nanostructure. As crosslinking in the majority phase becomes more significant, the matrix begins to densify, and the polymer domains decrease slightly in size, as described in Scheme S1.†38 We note that upon crosslinking, the degree of ordering of SEBS may be reduced, while the domain spacing expands from 21.0 to 40.2 nm. This is confirmed by the broadening of the primary scattering peak and a shift in peak position toward lower q values, as depicted by small angle X-ray

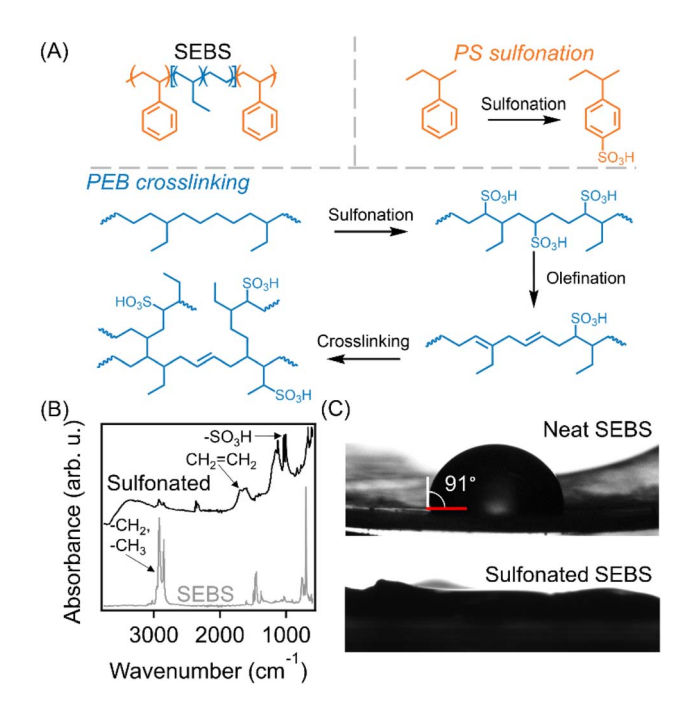


Fig. 1 (A) Mechanisms of two distinct reactions that occur in the PEB majority phase and PS minority phase of the SEBS precursor during the sulfonation-induced crosslinking. (B) FTIR spectroscopy results before and after sulfonation, indicating the consumption of the alkyl stretching vibrations between 2920 cm⁻¹ and 2850 cm⁻¹, as well as the addition of double bonds (1601 cm⁻¹) and sulfonic acids $(1030 \text{ cm}^{-1}, 1010 \text{ cm}^{-1})$. (C) Water contact angle measurements of the SEBS precursor before and after sulfonation-induced crosslinking.

scattering (SAXS) patterns in Fig. S1.† Fourier transform infrared (FTIR) spectroscopy results shown in Fig. 1(B) confirm the progress of the SEBS sulfonation reaction. First, intensity of bands between 2920 cm⁻¹ and 2850 cm⁻¹ were significantly reduced after crosslinking, indicating the consumption of alkyl hydrogens along the PEB backbone. Additionally, the appearance of alkene stretching vibrations at 1601 cm⁻¹ indicate the formation of double bonds, and bands at 1030 cm⁻¹ and 1010 cm⁻¹ represent the addition of the sulfonic acid groups along the PEB backbone and PS repeat unit, respectively. With the addition of these sulfonic acid groups, the crosslinked SEBS precursor becomes very hydrophilic, as indicated by water contact angle measurements (Fig. 1(C)). A water contact angle of $91 \pm 2^{\circ}$ is observed in the neat SEBS polymer, while the sulfonated SEBS can be completely wetted by the water droplet due to the significantly increased hydrophilicity, which is common in sulfonated polymer systems.42

A generalized scheme for preparing functionalized OMCs from the crosslinked SEBS precursors is presented in Fig. 2, including three distinct pathways for micropore activation, heteroatom doping, and the incorporation of metal nanoparticles, respectively. After crosslinking, the SEBS precursor can be pyrolyzed at 800 °C in an inert atmosphere, leading to the formation of OMC. The resulting OMCs can be chemically activated using potassium hydroxide (KOH) at 700 °C under nitrogen, which reacts and partially etches the carbon

framework to form micropores, resulting in an enhanced surface area; this method is similar to previous reports of postactivation of OMCs prepared from a soft-templating method.24,43 Additionally, the crosslinked SEBS precursor can be employed to impart additional chemical functionality into the final carbon products. Specifically, the crosslinked precursor can be physically blended with various heteroatom dopants prior to carbonization, resulting in the integration of heteroatoms (such as boron, nitrogen, phosphorus, and sulfur) into the carbon framework. The presence of these heteroatoms in the carbonized product provides an opportunity to alter the affinity between guest molecules and pore surfaces, thus potentially enhancing their performance in many applications such as CO2 capture and energy storage. 44-46 Additionally, the hydrophilic nature of the crosslinked SEBS can be leveraged to introduce water-soluble metal nitrates into the nanostructured OMC precursor, leading to the formation of nanoparticlecontaining OMCs directly from pyrolysis of crosslinked sulfonated SEBS.

Activation

Many applications of nanoporous carbons require a high surface area to maximize interactions between guest molecules and the carbon matrix.⁴⁷ For example, Gadipelli et al. demonstrated the synthesis of high surface area microporous carbon using pinecones as biomass precursors, which leads to tunable surface areas upon varying the processing conditions.48 These carbon materials exhibited improved sorption performance of CO₂, H₂, and water molecules with higher surface areas due to the increased availability of active adsorption sites. In general, activation of carbon requires etching the framework to encourage the formation of micropores, which, in turn, can lead to increased surface area of the material and promote sorption. In our work, activation was accomplished through physically blending the SEBS-derived OMCs with KOH at varied ratios, followed by a high temperature calcination treatment at 700 °C in a nitrogen atmosphere.49

Nitrogen physisorption measurements were performed to quantify the change in pore characteristics before and after the activation process. Specifically, the changes in Brunauer-Emmett-Teller (BET) surface area and average pore size determined through non-local density functional theory (NLDFT) from the adsorption isotherms are presented in Fig. 3(A). The sorption isotherm, pore size distribution, and scanning electron microscopy (SEM) image of the OMC prior to activation can be found in Fig. S2,† while the physisorption isotherms and pore size distributions after different activation treatment are included in Fig. S3 and S4,† respectively. The initial OMC prior to activation has a surface area of 485 m^2 g^{-1} and an averaged pore size of 12.9 nm. After activation reaction with KOH at mass ratios of 1:1, 2:1, 3:1, and 4:1 (KOH:carbon), the pore characteristics of the derived OMC change significantly. At a 1: 1 ratio, the surface area increases to 645 m² g⁻¹ and the pore size slightly decreases to 11.4 nm, which is likely a result of pore shrinkage from the extended exposure to high temperatures leading to reduced pore size. Increasing the amount of KOH for

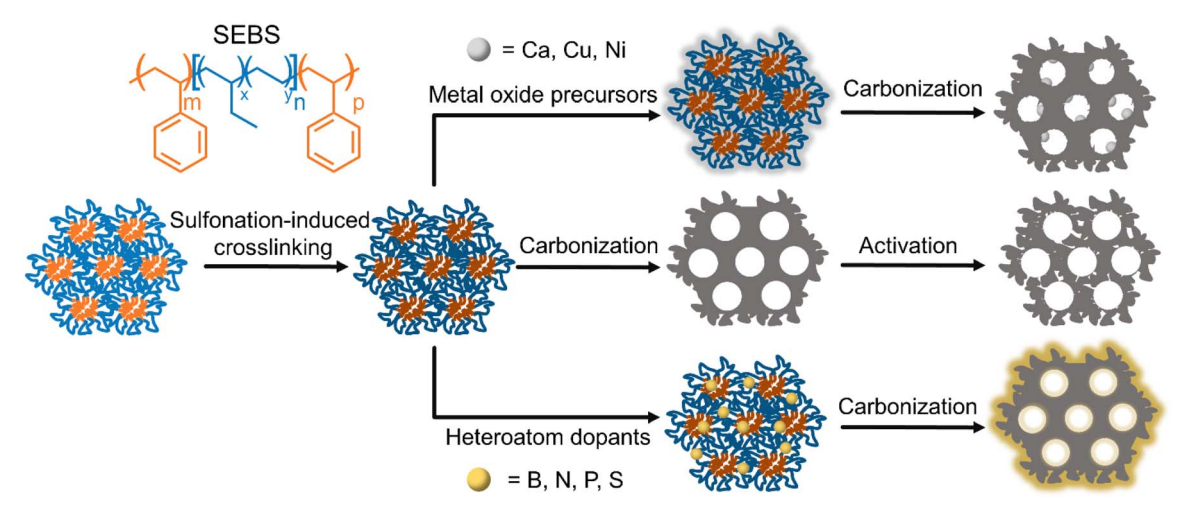


Fig. 2 Schematic illustration of TPEs acting as a platform precursor for the versatile functionalization of OMCs. High surface area, heteroatomdoped, or metal nanoparticle loaded OMCs can be synthesized through employing various techniques.

activation reaction results in increased surface areas, where at a mass ratio of 4:1 the activated sample exhibits a surface area of 1260 m² g⁻¹, which is more than double the surface area of the control system. Additionally, increasing the KOH: carbon ratio from 1:1 to 2:1, 3:1, and 4:1 results in pore sizes which are similar to the control sample prior to activation. This observation can be rationalized by considering the effects of the etching process on the pore structure itself. While the high temperatures required by the activation process can result in decreased pore size due to shrinkage of the carbon framework (as demonstrated by the sample activated at a 1:1 mass ratio), the increased amount of framework etching through activation effectively increases the pore size through etching away portions of the pore wall. Similar results have been previously observed

in soft-templated OMC systems with an initial surface area of 660 m² g⁻¹, which was increased to 1410 m² g⁻¹ after KOH activation. The change in pore sizes upon KOH activation were dictated by competition between the shrinkage of the carbon framework and etching the walls of the mesopores.24

Fig. 3(B) depicts SAXS patterns of the materials before and after KOH activation. The presence of the primary scattering peak indicates that ordered porous structures is retained upon the activation process. A similar trend to the variations in pore size is observed for the domain spacing with altered KOH to OMC ratio. Initially, the domain spacing decreases to 25.5 nm after activation at a 1:1 KOH to carbon mass ratio, compared to 28.4 nm in the pristine OMC sample. With higher amounts of KOH present during activation, the domain spacings increase to

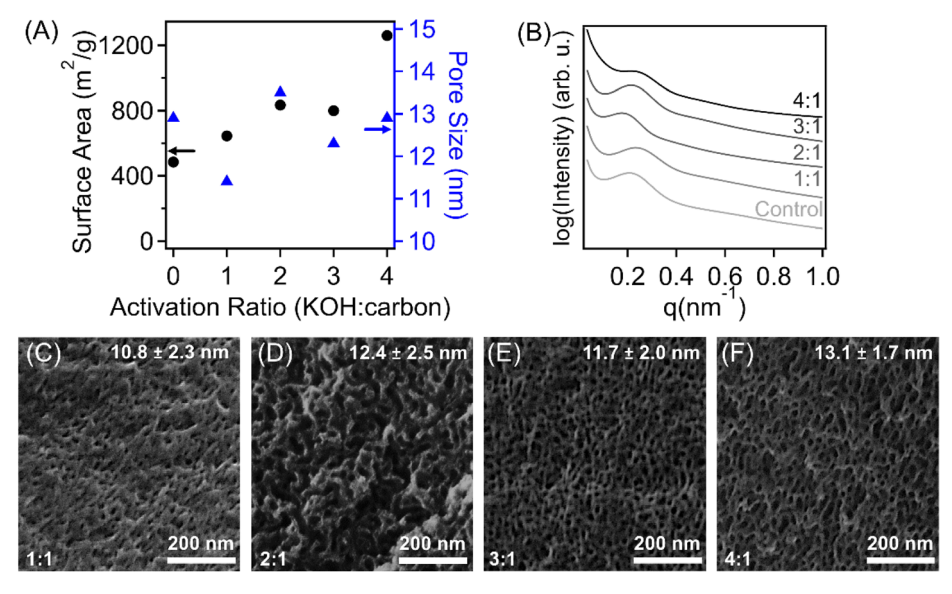


Fig. 3 (A) Effect of increased amount of KOH during activation on the BET surface area and pore size of the activated OMCs. (B) SAXS results of the activated OMCs before and after activation with varying KOH: carbon mass ratios. SEM images of TPE-derived OMCs after activation with KOH: carbon mass ratios of (C) 1:1, (D) 2:1, (E) 3:1, and (F) 4:1.

 \sim 27.8 nm, which is similar to the non-activated, control OMC samples. The increase in pore size with reduced domain spacing in these activated samples indicates that the activation step can expand mesopores while shrinking the thickness of carbon walls. Additionally, the etching reaction of the carbon matrix leads to increased full width at half maxima (FWHM) of the primary scattering peak with higher KOH content during activation. Specifically, the FWHM increases from 0.09 nm⁻¹ in the control sample prior to activation to 0.11 nm⁻¹ in the sample that was activated with a 4:1 ratio of KOH: carbon. This result indicates that the activation process can lead to a slight loss in the degree of ordering of the OMCs. Additionally, we note that the enhanced surface area in OMCs from an activation process can be useful for many different applications, such as energy storage and water remediation. Moreover, as shown in Fig. 3(C-F), SEM images confirm that the ordered nanostructures of the porous materials can be retained after activation, further supporting results from nitrogen physisorption isotherms and SAXS measurements. The averaged pore size determined from these SEM images were 10.8 \pm 2.3 nm, 12.4 \pm 2.5 nm, 11.7 \pm 2.0 nm, and 13.1 \pm 1.7 nm for samples activated at KOH to OMC ratios of 1:1, 2:1, 3:1, and 4:1, respectively.

Additionally, the activation process can also alter the surface functionality of the carbon materials through the addition of various oxygen containing functionalities. XPS spectroscopy was employed to investigate the effect of activation on the chemical composition of the SEBS-derived OMCs. The survey scan of the OMC prior to functionalization and the results for the samples activated with KOH at various carbon to KOH mass ratios are found in Fig. S5 and S6,† respectively. The sulfonation-induced crosslinking process inherently dopes the SEBS-derived OMCs with \sim 2.9 at% oxygen and \sim 0.3 at% sulfur prior to functionalization. After activating the samples with a mass ratio of 1:1 KOH to carbon, the oxygen content increases significantly to 11.6 at% while maintaining a sulfur content of 0.2 at%. The oxygen content increases with increasing KOH to carbon mass ratio, which reached an oxygen content of 19.3 at% after a 4:1 mass ratio of KOH: OMC. It is also noted that the activation process results in small amounts (<2 at%) of potassium which could be a result of adsorbed ions or various potassium containing surface functionalities. The increase in oxygen containing functionalities with large mass ratios of KOH to carbon has been observed in many different carbon systems and has been demonstrated to improve their utility for applications like supercapacitors. 50,51

Heteroatom doping

The incorporation of heteroatoms into OMCs has been demonstrated as an effective method to improve their performance in different applications, such as energy storage or molecular separations, through tuning interactions between the carbon matrix and guest molecules. This can be accomplished through pyrolysis of heteroatom-containing OMC precursors, or the inclusion of heteroatom dopants during the carbonization process. 52,53 A previous work reported a universal strategy to dope a soft-templated polymer–silica composite

system through a melt-diffusion approach, involving physical blending of dopants and porous polymer precursors and a subsequent step of carbonization.⁵⁴ In our process of preparing SEBS-derived OMCs, use of sulfonation-induced crosslinking chemistry leads to incorporation of sulfur heteroatom into the precursors, which can be retained upon pyrolysis and lead to the formation of sulfur-doped OMCs. 55,56 Here, to further enhance the utility of these OMCs while expanding accessible framework chemistry to include different heteroatoms, we show that doping SEBS-derived OMCs can be accomplished by pyrolysis of crosslinked SEBS blended with the presence of heteroatom dopants of varying chemical identity. This method can lead to tailored chemical functionality of the carbon matrix, while it is distinct from the previous report which infiltrated doping agents into a porous polymer framework.54 Here we note that we first attempted infiltrating dopants into the porous SEBS, which was prepared through thermal degradation of PS minority domains at 400 °C and subsequent infiltration of the dopants through physical blending and calcination. However, this resulted in very minimal doping levels and a complete loss of ordered structures indicated by the absence of hysteresis in the nitrogen physisorption isotherm (Fig. S7†).

Boric anhydride, melamine, ammonium dihydrogen phosphate, and dibenzyl disulfide were employed as the dopants for boron, nitrogen, phosphorus, and sulfur heteroatoms, respectively. The blends, including crosslinked SEBS and dopant at a mass ratio of 1:1, were then carbonized at 800 °C to form heteroatom-doped OMC products. XPS survey scans (Fig. 4(A-D)) depict the efficacy of this doping method, as well as the bonding environments of the individual heteroatoms. Physically blending crosslinked SEBS with the heteroatom dopants at a 1:1 mass ratio results in the incorporation of 0.7 at%, 3.3 at%, 7.0 at% and 3.5 at% for boron, nitrogen, phosphorus, and sulfur, respectively. As previously discussed, the sulfonationinduced crosslinking process inherently dopes the carbon framework and therefore up to 1 at% sulfur is present in all samples, except for the OMC doped with dibenzyl disulfide which contains a higher sulfur doping content. In a previous work,54 a porous polymer/silica composite was infiltrated with the dopants at elevated temperatures and, at a 1:1 mass ratio of dopant to mesoporous precursor, XPS results indicated doping contents of 3.4 at%, 18.8 at%, 0.8 at%, and 0.7 at% for boron, nitrogen, phosphorus, and sulfur, respectively. As shown in Fig. 4, the incorporation of phosphorus and sulfur is much more efficient in SEBS-derived OMCs, while the doping levels of boron and nitrogen are greatly reduced. Generally, boron doping levels in carbon materials can be low due to reduced reactivity of boron-containing dopants.⁵⁷ Additionally, for the nitrogen-doped material, the lower doping content could be due to the reduced miscibility between relatively hydrophobic melamine and the hydrophilic crosslinked SEBS, which may limit the efficient diffusion of melamine dopant (which has a melting temperature of approximately 340 °C) during the carbonization process. To that point, it is found that the hydrophilic dopant, such as dihydrogen ammonium phosphate resulted in very efficient co-doping of phosphorus and nitrogen

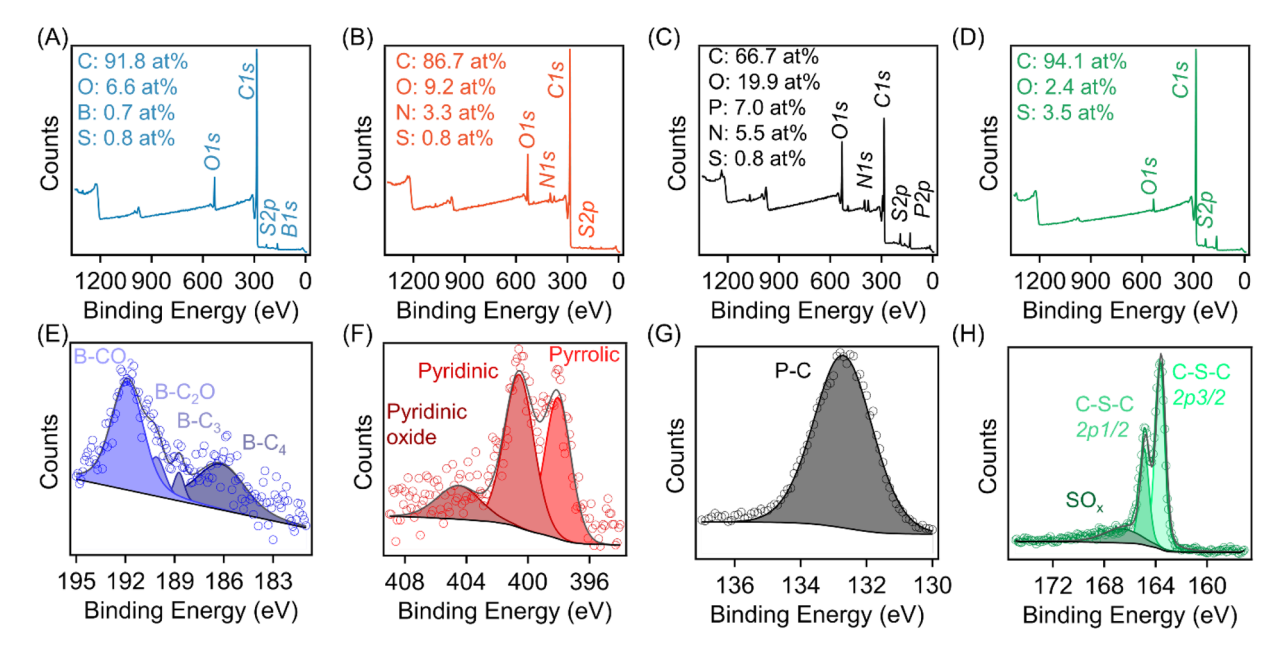


Fig. 4 XPS survey scans for (A) boron, (B) nitrogen, (C) phosphorus, and (D) sulfur doped OMCs. High resolutions scans depicting the bonding environments of (E) boron, (F) nitrogen, (G) phosphorus, and (H) sulfur heteroatoms.

heteroatoms in our method. This efficiency may stem from favorable ionic interactions between the sulfonic acid groups within the crosslinked SEBS and the positively charged ammonium species within the ammonium dihydrogen phosphate dopant, ultimately increasing miscibility and overall incorporation of the heteroatom into the carbon framework.

We note that the efficacy of our doping method is comparable with other established approaches for preparing doped-OMCs. For example, Yu et al. synthesized OMCs through a soft-templating approach, employing urea as a nitrogen dopant to cooperatively self-assemble with carbon precursors during OMC synthesis.58 This method resulted in similar nitrogen contents to the approach reported in our work with \sim 3 at% nitrogen in the carbon materials. Similarly, Liu et al. used nitrogen-containing carbon precursors to synthesize nitrogendoped OMCs through a cooperative-assembly, involving the use of 3-aminophenol as the nitrogen dopant.⁵⁹ It was reported that a maximum of 3.6 at% nitrogen was obtained in the OMC products. Additionally, it is worth noting that there is a potential opportunity to increase doping levels in these materials through employing higher ratios of dopant to precursors. However, increasing the doping content may lead to compromised degree of ordering within the carbon nanostructure. It is also worth noting that the phosphorus content in this work is significantly higher than other instances in the literature which employ exogenous phosphorus containing dopants. 60-62

In addition to characterizing doping contents, the bonding environments of the heteroatoms were investigated through performing high-resolution XPS scans, which are presented in Fig. 4(E–H). The B 1s scan (Fig. 4(E)) of the boron-doped carbon exhibits 4 peaks that describe the resulting boron bonding environment. These peaks are located at 191.9 eV, 190.1 eV, 188.7 eV, and 186.3 eV which correspond to B–CO₂, B–C₂O, B–

C₃, and B-C₄, respectively.^{63,64} These assignments indicate that doping boron into the carbon framework results in the formation of both oxygen containing species, as well as incorporation directly into the carbon framework, where the oxygen containing species are major components. The enhanced doping level of B-C-O species may prove useful; for example, it has been previously demonstrated that the increased presence of B-C-O species can provide active sites which result in enhanced surface adsorption of Na⁺ ions and rapid Na⁺ ion diffusion, thus providing elevated performance in sodium ion battery.65 The nitrogen-doped sample contains multiple bonding environments for N including pyridinic nitrogen (398.1 eV, ~45 at%), pyrrolic nitrogen (400.5 eV, ~35 at%), as well as a population of pyridinic oxides (404.4 eV, ~19 at%),66,67 while, interestingly, graphitic N heteroatoms were not observed in this sample. The preferential formation of pyridinic and pyrrolic functionalities in nitrogen-doped carbons is consistent with previous studies.54,68 Notably, the incorporation of nitrogen heteroatoms into carbon materials represents a common approach to enhance their performance in various applications, including but not limited to, CO2 capture and heterogeneous catalysis.69 In the phosphorus-doped material, a single peak is present at 132.7 eV in the P 2p high-resolution scan corresponding to a P-C bonding environment, 70 which may lead to improved performance for metal-free electrocatalysts for oxygen reduction reaction (ORR). Specifically, incorporating phosphorus atoms into the carbon frameworks results in the formation of P-C bonds which are longer in length than C-C bonds. Consequently, a defect site is formed which can act as a site for adsorbing O2 to promote ORR.60 The S 2p scan of the sample doped with dibenzyl disulfide indicates the presence of two different bonding environments that result from the doping process. The majority of the sulfur (~93 at%) exists as C-S-C

bonds that have been directly incorporated into the carbon framework, while there is a broad peak present that indicates the presence of various SO_x containing functionalities (\sim 7 at%), which could be a result of the oxidation of sulfur containing functionalities during the carbonization process. The SEBS-derived OMC, before undergoing functionalization, already contains \sim 0.3 at% of sulfur (Fig. S5†), introduced during the sulfonation-induced crosslinking step. This sulfonation crosslinking-enabled inherent sulfur doping primarily results in the formation of C–S–C bonds, with the absence of SO_x functional groups, as evidenced by the high resolution scant in Fig. S8.†

It has been previously determined that doping ordered mesoporous carbons (OMCs) with heteroatoms significantly affects their pore nanostructure, notably influencing the degree of ordering and domain spacing. The impact of heteroatom doping on the OMC nanostructure was quantitatively studied through SAXS and nitrogen physisorption measurements depicted in Fig. 5. All the SAXS patterns contain a primary scattering peak, indicating that the ordered nanostructures were retained after simultaneous doping and carbonization reactions. The domain spacings of the samples doped with boron, nitrogen, sulfur, and phosphorus are 30.3 nm, 28.7 nm, 32.2 nm, and 26.3 nm, respectively. All the doped carbons, with the exception of the phosphorus doped sample, exhibit increased domain spacings compared to the neat, undoped samples which is a result of the larger heteroatoms incorporated into the carbon matrix swelling the pore walls. Additionally, the primary scattering peak becomes broader from doping reactions, indicating that the incorporation of heteroatoms can disrupt the degree of ordering within the nanostructure, especially in the case of the sulfur and nitrogen containing OMCs. Additionally, the sample doped with phosphorus exhibits the slight presence of a secondary scattering peak with a peak position at a ratio of $\sqrt{7}$ with respect to the primary scattering peak. This result is consistent with the anticipated presence of the ordered cylindrical nanostructure of OMC. Nitrogen physisorption isotherms of the doped materials are found in Fig. S9,† and their corresponding pore size distributions are shown in Fig. 5(B). Despite the decrease in the degree of nanostructure ordering as indicated by the SAXS patterns of the doped materials, NLDFT pore size distributions indicate nearly identical average pore sizes in the samples with fluctuations of

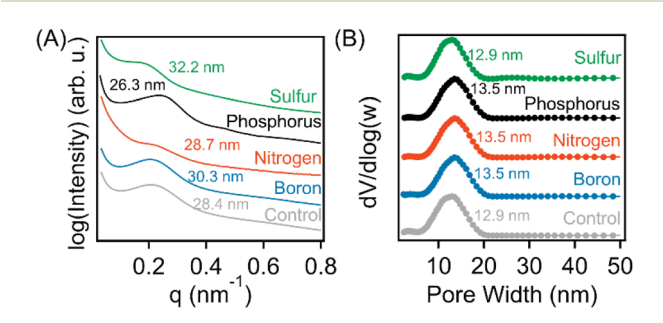


Fig. 5 (A) SAXS patterns and (B) NLDFT pore size distributions of the doped OMCs containing different heteroatoms.

less than 1 nm between all samples. These results indicate the incorporation of heteroatoms through this reported approach primarily alter the thickness of pore walls and has a relatively limited impact on the pore size, which is different from the method of cooperative assembly between carbon precursors and heteroatom dopants. Additionally, the surface areas of these doped OMC samples generally decrease after the incorporation of heteroatoms. The surface areas for the boron, nitrogen, phosphorus, and sulfur doped samples are 437 m² g⁻¹, 232 m² g⁻¹, 100 m² g⁻¹, and 82 m² g⁻¹, respectively. Decreases in surface area from the incorporation of heteroatoms have been demonstrated previously in the literature and are likely a result of disruption of microstructures from doping reactions.

Furthermore, SEM images in Fig. 6 provide a direct visualization of the pore nanostructures of doped samples. Across the boron-, nitrogen-, phosphorus-, and sulfur-doped samples, the SEM images indicate presence of the ordered mesopores within the OMCs. From image analysis, the doped samples have pore sizes of 14.6 \pm 2.9 nm, 13.0 \pm 1.9 nm, 13.2 \pm 2.4 nm, and 13.7 \pm 2.5 nm, for the OMCs doped with boron, nitrogen, phosphorus, and sulfur heteroatoms, respectively; these results are in good agreement with the pore sizes determined through physisorption measurements.

Metal nanoparticle-containing OMCs

The incorporation of metal nanoparticles into OMCs can greatly enhance their utility in applications such as catalysis and energy storage. For example, embedding metal nanoparticles into OMCs for use in heterogeneous catalysis takes advantage of the mesopore channels within the OMC structure to enhance the diffusion of larger molecules throughout the carbon matrix.74 This process allows reactant molecules to interact with the active metal species, which serve as catalytic sites, thereby facilitating chemical reactions.74 Metal nanoparticles can be incorporated into OMCs through various methods.75,76 In this work, the functional groups imparted into the crosslinked SEBS precursor enable the infiltration of metal precursors through favored interactions between metal ions and charged groups within the crosslinked SEBS. Specifically, metal nitrates dissolved in water can be easily introduced through a simple immersion step. Subsequently, the composites can be heated at 800 °C for 3 h to simultaneously carbonize the SEBS precursor and convert the metal nitrates into metal nanoparticles, which can be directly incorporated in the OMC framework. We demonstrate the generalizability of this approach using three model metal nitrates, including calcium nitrate tetrahydrate, copper nitrate hemipentahydrate, and nickel nitrate hexahydrate as metal nanoparticle precursors.

Thermogravimetric analysis (TGA) experiments were performed on the carbonized material in the air up to 800 °C to determine the amount of metal loaded into the OMCs as a function of metal nitrate solution concentration (Fig. 7(A)). Additionally, the corresponding TGA thermograms (performed under air) can be found in Fig. S10–S12† for calcium-, copper, and nickel-containing samples, respectively. We note that upon

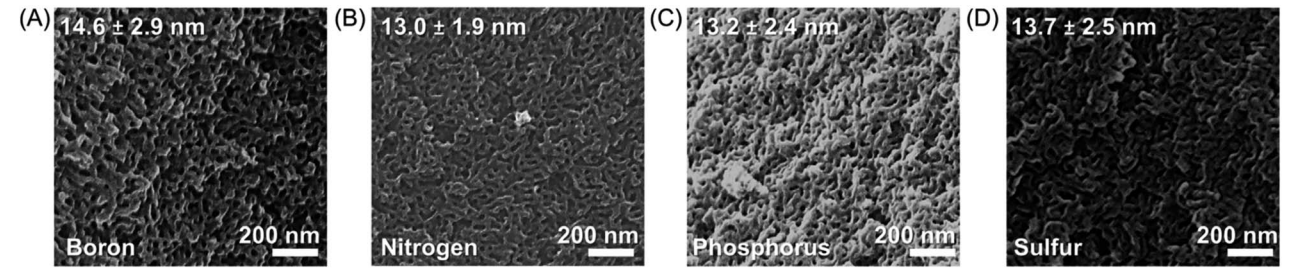


Fig. 6 SEM images of (A) boron-, (B) nitrogen-, (C) phosphorus-, (D) and sulfur-doped OMCs.

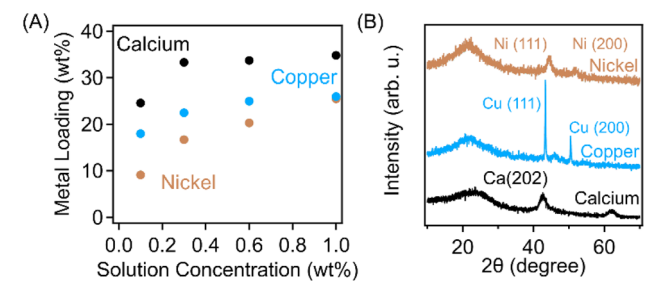


Fig. 7 (A) Metal loadings as a function of metal nitrate solutions concentration for calcium, copper, and nickel precursors determined through TGA. (B) Representative XRD patterns for calcium, copper, and nickel incorporated OMCs which had loadings of 35 wt%, 27 wt%, and 26 wt%, respectively.

calcination under air, carbon can be completely decomposed due to their oxidation reaction, while the residue mass from TGA measurements can be employed to determine the metal loading content. In our system, when the metal nitrate solution concentrations are as low as 0.1 wt%, the OMCs are loaded with 23 wt%, 18 wt%, and 9 wt% of calcium, copper, and nickel, respectively. These values approach maxima at solution concentrations of 1 wt%, reaching values of 35 wt%, 27 wt%, and 26 wt%, respectively. The crystalline structure of the metal species within the OMCs have been determined through X-ray diffraction (XRD), and representative patterns are found in Fig. 7(B). In both the nickel and copper samples, only Cu and Ni metallic species are suggested, without peaks that represent the presence of metal oxides. More specifically, peaks at 44.5° and 51.8° represent the (111) and (200) reflections for the metallic nickel species.77 The sample loaded with copper particles exhibits a peak at 43.3°, representing the (111) crystal plane, and another peak at 50.4°, which represents the (200) plane.78 While the carbonization process could be expected to form calcium oxides through the decomposition of calcium nitrate, these oxide species are highly sensitive to both CO2 and atmospheric moisture.79 As a result, the peaks present in the XRD results for the calcium loaded sample at 43.0° and 62.3° represent reflections of calcite polymorph of calcium carbonate.80 However, with high temperature chemical treatment, these can be converted back into the oxide form for further use. It is worth noting that the peaks in the diffraction pattern for the copper loaded sample are much more distinct than the other metal counterparts. When comparing this to the

nickel-loaded carbon, the increase in intensity of these peaks is likely a result of the lower melting temperature of copper compared to that of nickel. This lower temperature may allow copper to recrystallize more readily, thus resulting in a more intense diffraction pattern. Alternatively, the variation in the crystallinity of metal samples can also be attributed to the different formation mechanism and kinetics of nanoparticles from nitrate salts, although this aspect is not within the scope of this work. The calcium loaded sample has less distinct, broad diffraction peaks due to the numerous potential polymorphs of calcium carbonate that can exist. This results in broadened peaks with reduced scattering. The XRD results are also confirmed through XPS survey scans presented in Fig. S13.† First of all, we note that XPS survey scan is a surface and local measurement method, with a probing depth of \sim 5 nm. Therefore, the metal amount in OMC samples determined from XPS does not agree well with TGA measurements, with the latter being significantly more accurate. The survey scan for the calcium loaded sample indicates a single Ca 2p peak which corresponds to calcium carbonate species. Similarly, the survey scans of the copper and nickel samples exhibit peaks which correspond to the metallic species without the presence of oxides. Two peaks at 933 eV and 953 eV represent the Cu 2p_{3/2} and Cu 2p_{1/2} peaks of metallic copper species and a single peak at 853 eV corresponds to the 2p_{3/2} peak of metallic nickel species. Additionally, incorporating the metal nanoparticles into the carbon products results in increased heteroatom contents. The calcium loaded sample exhibits significantly increased oxygen and sulfur contents, in addition to the presence of nitrogen, which is likely the result of portions of the metal nitrate precursor being incorporated into the carbon framework during the pyrolysis process. The copper and nickelloaded materials only exhibit slightly increased sulfur and oxygen contents, without the incorporation of nitrogen heteroatoms.

SEM images of the metal incorporated OMCs in Fig. 8 depict the retention of the ordered porous nanostructure of the SEBSderived OMCs with the incorporation of metal nanoparticles. As a note, the images in Fig. 8 are from samples all after incorporation from metal nitrate solution concentrations of 0.1 wt%. From image analysis, the calcium, copper, and nickel nanoparticle incorporated exhibit average pore sizes of 12.0 \pm 2.0 nm, 12.0 \pm 2.3 nm, and 13.3 \pm 2.7 nm, respectively. These results indicate only slight changes in pore sizes even after

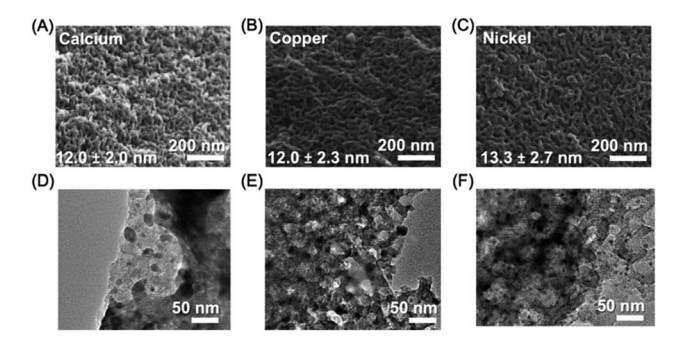


Fig. 8 SEM images of (A) calcium, (B) copper, and (C) nickel nanoparticle incorporated OMCs after loading from 0.1 wt% metal nitrate solutions. Corresponding TEM images illustrating the presence of (D) calcium, (E) copper, and (F) nickel nanoparticles within the OMCs.

loading significant weight fractions of metal nanoparticles into the carbon framework. Importantly, the TEM images in Fig. 8(D–F) directly visualize the presence of nanoparticles within the OMCs. Despite very high loadings of the metal species, the nanoparticles remain relatively small (17.2 \pm 4.1 nm in diameter for calcium-based nanoparticles, 11.3 \pm 2.7 nm in diameter for copper-based nanoparticles, and 5.0 \pm 0.8 nm in diameter for nickel-based nanoparticles), which can be useful for applications as they reduce pore blockage and optimize the amount of area available for interactions with molecules of interest. $^{\rm s1}$

The effect of the metal nanoparticle loading on the pore texture and nanostructure of the OMCs is characterized through physisorption measurements and SAXS in Fig. 9. For OMC containing calcium nanoparticles, it is observed that the pore size remains relatively constant despite the amount of metals loaded within the pores of the material (Fig. S14†), and the surface area remains relatively constant until decreasing from

485 m² g⁻¹ to 330 m² g⁻¹ from using 1 wt% concentration of metal nitrate solution, leading to a loading level of \sim 35 wt%. Interestingly, the surface area of the copper nanoparticle loaded OMCs (Fig. 9(B)) is lower than the control OMC, but can increase with higher loading content of the metal nanoparticles. This could potentially be a result of chemical activation process from the decomposing metal precursor etching micropores into the carbon matrix. However, in copper nanoparticle loaded samples, the average pore size fluctuates between 9 and 13 nm and decreases with increasing solution concentration. This could be a result of the formation of the large nanoparticles, as depicted in Fig. 8(E) resulting in more pore blocking and decreasing the pore size through physisorption measurements. Interestingly, the pore size distributions for the copper and nickel loaded OMCs (Fig. S15 and S16†) exhibit a secondary peak after loading with the inorganic nanoparticles. The second peak at smaller pore sizes could be arise from pores that have become blocked by the inorganic nanoparticles, thus artificially decreasing the detected pore size through physisorption measurements. In addition to understanding the impact of incorporating nanoparticles on the pore texture, SAXS patterns depict how the global nanostructure of the resulting OMC changes, which can be found in Fig. 9(D-F). The corresponding domain spacings extracted from the primary scattering peak are found in Table S1.† All of the domain spacings are relatively similar regardless of the metal loading content, which vary between 27.8 nm and 31.6 nm. Additionally, the domain spacings of these metal nanoparticle containing samples are generally close to that of the OMC prior to functionalization, which indicates that the metal loading process does not result in significant swelling of the porous carbon nanostructure upon carbonization. It is also worth noting that there seems to be a slight secondary scattering peak in most of the samples in the scattering pattern. However, these secondary

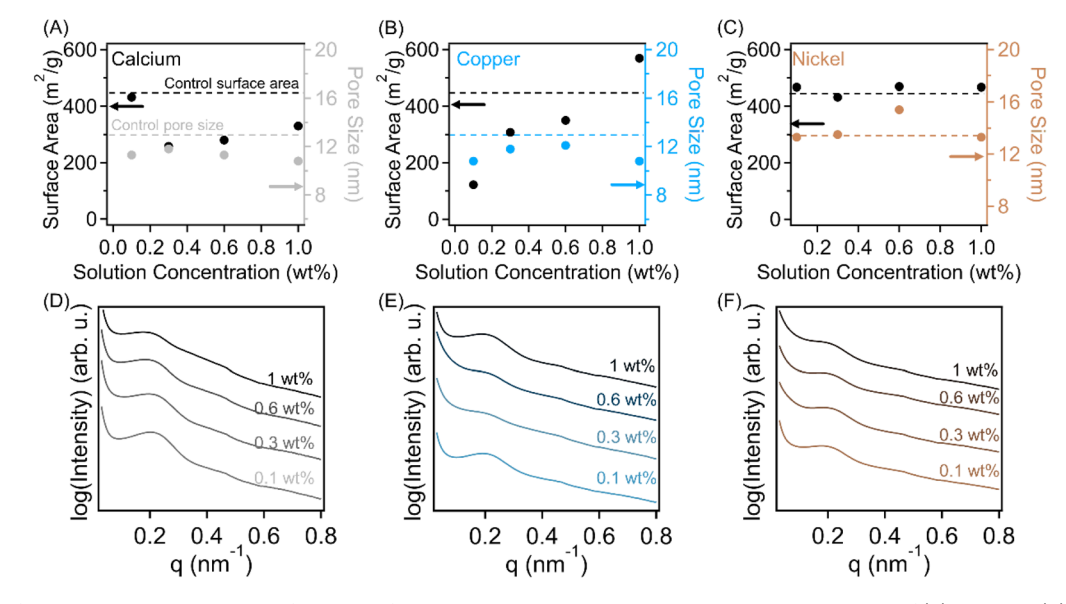


Fig. 9 OMC surface area and pore size as a function of metal nitrate solution concentration during loading of (A) calcium, (B) copper, (C) and nickel species. SAXS patterns of the resulting carbons after loading with (D) calcium, (E) copper, and (F) nickel.

peaks are all very broad, making it challenging to use them for characterizing the nanostructure of the samples.

Conclusions

Development of simple and scalable processing methods for enhancing the utility of TPE-derived OMCs is important for enabling their widespread adoption across many applications. The synthetic method for fabricating TPE-derived OMCs provides an excellent potential for scaled OMC synthesis compared to conventional strategies. In this work, we demonstrate several simple functionalization methods which can be employed to tune the characteristics of the carbon products. Specifically, it is observed that chemical activation of OMC with KOH can increase the surface area of the materials by twice that of the original material (1260 m² g⁻¹ compared to 485 m² g⁻¹). Additionally, blending the crosslinked SEBS with various dopants can lead to the in situ incorporation of heteroatoms into the carbon framework upon pyrolysis, which can enable improved performance and functionalities for adsorption and energy storage applications. Boron, nitrogen, sulfur, and phosphorus are all effectively incorporated into the carbon materials, while the ordered pore structures can be retained. Moreover, the hydrophilic nature of the crosslinked SEBS precursor is leveraged to incorporate water soluble metal nitrates into the polymer network which are converted to metal nanoparticles upon carbonization. Nanosized calcium, nickel, and copper particles can be formed and dispersed into the carbon frameworks which could greatly impact their performance for applications in heterogeneous catalysis. Overall, this work demonstrates straightforward strategies for tailoring the chemical functionality and pore texture of the TPE-derived OMCs, which can be leveraged to enhance their utility for various applications.

Data availability

The data supporting this article have been included as part of the ESI.†

Author contributions

M. R. and Z. Q. devised the experimental design for this work, while A. B. and A. G. assisted M. R. in material preparation and characterization. J. A. and D. P. performed XPS experiments, and Y. X. assisted with XRD and TEM characterization. Z. Q. oversaw the completion of the experiments. The manuscript was written through contributions of all authors.

Conflicts of interest

There are no conflicts to declare regarding this work.

Acknowledgements

This work is supported by the U.S. National Science Foundation under grant CMMI-2239408. This research used beamline 11BM of the National Synchrotron Light Source II, a U.S. Department of Energy (DOE) Office of Science User Facility operated for the DOE Office of Science by Brookhaven National Laboratory under Contract No. DE-SC0012704. The authors would like to acknowledge the beamline scientists Dr Ruipeng Li and Dr Feipeng Yang for their assistance during scattering experiments.

References

- 1 T. Yamamoto, S. I. Kim, J. Chaichanawong, E. ua Apiluck and T. Ohmori, Removal of Aqueous Organic Pollutants by Adsorption-Catalytic Process Using Mesoporous Carbon Beads Loaded with Metal Oxides, Appl. Catal., B, 2009, 88, 455-461
- 2 M. Park, S. Wu, I. J. Lopez, J. Y. Chang, T. Karanfil and S. A. Snyder, Adsorption of Perfluoroalkyl Substances (PFAS) in Groundwater by Granular Activated Carbons: Hydrophobicity of PFAS Characteristics, Water Res., 2020, 170, 115364.
- 3 Y. Wan, H. Wang, Q. Zhao, M. Klingstedt, O. Terasaki and D. Zhao, Ordered Mesoporous Pd/Silica-Carbon as a Highly Active Heterogeneous Catalyst for Coupling Reaction of Chlorobenzene in Aqueous Media, J. Am. Chem. Soc., 2009, 131, 4541-4550.
- 4 R. Liu, X. Wang, X. Zhao and P. Feng, Sulfonated Ordered Mesoporous Carbon for Catalytic Preparation of Biodiesel, Carbon, 2008, 46, 1664-1669.
- 5 Z. Bao, M. K. Song, S. C. Davis, Y. Cai, M. Liu and K. H. Sandhage, High Surface Area, Micro/Mesoporous **Particles** with Selectable 3-D Biogenic Morphologies for Tailored Catalysis, Filtration, Adsorption, Energy Environ. Sci., 2011, 4, 3980-3984.
- 6 Q. Zhao, Y. Lin, N. Han, X. Li, H. Geng, X. Wang, Y. Cui and S. Wang, Mesoporous Carbon Nanomaterials in Drug Delivery and Biomedical Application, Drug Delivery, 2017, 24, 94-107.
- 7 M. Gisbert-Garzarán, J. C. Berkmann, D. Giasafaki, D. Lozano, K. Spyrou, M. Manzano, T. Steriotis, G. N. Duda, K. Schmidt-Bleek, G. Charalambopoulou and M. Vallet-Regí, Engineered PH-Responsive Mesoporous Carbon Nanoparticles for Drug Delivery, ACS Appl. Mater. Interfaces, 2020, 12, 14946-14957.
- 8 B. Zheng, X. Lin, X. Zhang, D. Wu and K. Matyjaszewski, Emerging Functional Porous Polymeric and Carbonaceous Materials for Environmental Treatment and Energy Storage, Adv. Funct. Mater., 2020, 30, 1907006.
- 9 J. N. Pagaduan, A. Bhardwaj, T. Y. McCarty, S. Kraemer, C. J. Kearney, J. J. Watkins, T. Emrick and R. Katsumata, Fabrication of Porous Heteroatom-Doped Carbon Networks via Polymer-Assisted Rapid Thermal Annealing, Adv. Funct. Mater., 2024, 34, 2310296.
- 10 Z. Qiang, Y. M. Chen, Y. Xia, W. Liang, Y. Zhu and B. D. Vogt, Ultra-Long Cycle Life, Low-Cost Room Temperature Sodium-Sulfur Batteries Enabled by Highly Doped (N,S) Nanoporous Carbons, Nano Energy, 2017, 32, 59-66.

- 11 L.-C. Sang, A. Vinu and M.-O. Coppens, General Description of the Adsorption of Proteins at Their Iso-Electric Point in Nanoporous Materials, *Sep. Purif. Technol.*, 2011, 27, 13828–13837.
- 12 M. Trojanowicz, A. Bojanowska-Czajka, I. Bartosiewicz and K. Kulisa, Advanced Oxidation/Reduction Processes Treatment for Aqueous Perfluorooctanoate (PFOA) and Perfluorooctanesulfonate (PFOS) – A Review of Recent Advances, Chem. Eng. J., 2018, 336, 170–199.
- 13 R. Ryoo, S. H. Joo, M. Kruk and M. Jaroniec, Ordered Mesoporous Carbons, *Adv. Mater.*, 2001, 13, 677–681.
- 14 T. Y. Ma, L. Liu and Z. Y. Yuan, Direct Synthesis of Ordered Mesoporous Carbons, *Chem. Soc. Rev.*, 2013, 42, 3977–4003.
- 15 M. Robertson, M. M. Zagho, S. Nazarenko and Z. Qiang, Mesoporous Carbons from Self-Assembled Polymers, J. Polym. Sci., 2022, 60, 2015–2042.
- 16 Y. Meng, D. Gu, F. Zhang, Y. Shi, L. Cheng, D. Feng, Z. Wu, Z. Chen, Y. Wan, A. Stein and D. Zhao, A Family of Highly Ordered Mesoporous Polymer Resin and Carbon Structures from Organic-Organic Self-Assembly, *Chem. Mater.*, 2006, 18, 4447–4464.
- 17 Z. Zhou, T. Liu, A. U. Khan and G. Liu, Block Copolymer–Based Porous Carbon Fibers, *Sci. Adv.*, 2019, 5, eaau6852.
- 18 Z. Qiang, Y. Guo, H. Liu, S. Z. D. Cheng, M. Cakmak, K. A. Cavicchi and B. D. Vogt, Large-Scale Roll-to-Roll Fabrication of Ordered Mesoporous Materials Using Resol-Assisted Cooperative Assembly, ACS Appl. Mater. Interfaces, 2015, 7, 4306–4310.
- 19 M. Zhong, E. K. Kim, J. P. Mcgann, S.-E. Chun, J. F. Whitacre, M. Jaroniec, K. Matyjaszewski and T. Kowalewski, Electrochemically Active Nitrogen-Enriched Nanocarbons with Well-Defined Morphology Synthesized by Pyrolysis of Self-Assembled Block Copolymer, *J. Am. Chem. Soc.*, 2012, 134, 14846–14857.
- 20 M. J. Lázaro, L. Calvillo, E. G. Bordejé, R. Moliner, R. Juan and C. R. Ruiz, Functionalization of Ordered Mesoporous Carbons Synthesized with SBA-15 Silica as Template, *Microporous Mesoporous Mater.*, 2007, 103, 158–165.
- 21 H. Liu, Y. Zhang, Q. Ke, K. H. Ho, Y. Hu and J. Wang, Tuning the Porous Texture and Specific Surface Area of Nanoporous Carbons for Supercapacitor Electrodes by Adjusting the Hydrothermal Synthesis Temperature, *J. Mater. Chem. A*, 2013, **1**, 12962–12970.
- 22 M. Enterría and J. L. Figueiredo, Nanostructured Mesoporous Carbons: Tuning Texture and Surface Chemistry, *Carbon*, 2016, **108**, 79–102.
- 23 J. Ludwinowicz and M. Jaroniec, Effect of Activating Agents on the Development of Microporosity in Polymeric-Based Carbon for CO2 Adsorption, *Carbon*, 2015, 94, 673–679.
- 24 Y. Lv, F. Zhang, Y. Dou, Y. Zhai, J. Wang, H. Liu, Y. Xia, B. Tu and D. Zhao, A Comprehensive Study on KOH Activation of Ordered Mesoporous Carbons and Their Supercapacitor Application, J. Mater. Chem., 2012, 22, 93–99.
- 25 Y. Gao, Q. Wang, G. Ji, A. Li and J. Niu, Doping Strategy, Properties and Application of Heteroatom-Doped Ordered Mesoporous Carbon, *RSC Adv.*, 2021, **11**, 5361–5383.

- 26 J. Zhang, G. Chen, Q. Zhang, F. Kang and B. You, Self-Assembly Synthesis of N-Doped Carbon Aerogels for Supercapacitor and Electrocatalytic Oxygen Reduction, ACS Appl. Mater. Interfaces, 2015, 7, 12760–12766.
- 27 A. Griffin, N. Smith, M. Robertson, B. Nunez, J. McCraw, H. Chen and Z. Qiang, Research Experiences *via* Integrating Simulations and Experiments (REVISE): A Model Collaborative Research Project for Undergraduate Students in CO2 Sorbent Design, *J. Chem. Educ.*, 2024, **101**, 1096–1105.
- 28 Z. Qiang, Y. M. Chen, B. Gurkan, Y. Guo, M. Cakmak, K. A. Cavicchi, Y. Zhu and B. D. Vogt, Cooperatively Assembled, Nitrogen-Doped, Ordered Mesoporous Carbon/ Iron Oxide Nanocomposites for Low-Cost, Long Cycle Life Sodium-Ion Batteries, *Carbon*, 2017, 116, 286–293.
- 29 Y. Liu, Y. Xiong, P. Xu, Y. Pang and C. Du, Enhancement of Pb(II) Adsorption by Boron Doped Ordered Mesoporous Carbon: Isotherm and Kinetics Modeling, *Sci. Total Environ.*, 2020, **708**, 134918.
- 30 Y. Wang, H. Zhao and G. Zhao, Iron-Copper Bimetallic Nanoparticles Embedded within Ordered Mesoporous Carbon as Effective and Stable Heterogeneous Fenton Catalyst for the Degradation of Organic Contaminants, *Appl. Catal., B*, 2015, **164**, 396–406.
- 31 H. Jiang, J. Ma and C. Li, Mesoporous Carbon Incorporated Metal Oxide Nanomaterials as Supercapacitor Electrodes, *Adv. Mater.*, 2012, 24, 4197–4202.
- 32 Y. Lin, X. Wang, G. Qian and J. J. Watkins, Additive-Driven Self-Assembly of Well-Ordered Mesoporous Carbon/Iron Oxide Nanoparticle Composites for Supercapacitors, *Chem. Mater.*, 2014, **26**, 2128–2137.
- 33 N. C. Kovach, G. A. Russell-Parks and B. G. Trewyn, Strategies for Post-Synthetic Functionalization of Mesoporous Carbon Nanomaterial Surfaces, *Microporous Mesoporous Mater.*, 2022, 329, 111453.
- 34 Y. Zhai, Y. Dou, X. Liu, S. S. Park, C. S. Ha and D. Zhao, Soft-Template Synthesis of Ordered Mesoporous Carbon/ Nanoparticle Nickel Composites with a High Surface Area, *Carbon*, 2011, 49, 545–555.
- 35 W. Kou, Y. Zhang, J. Dong, C. Mu and L. Xu, Nickel-Nitrogen-Doped Three-Dimensional Ordered Macro-/Mesoporous Carbon as an Efficient Electrocatalyst for CO2 Reduction to CO, ACS Appl. Energy Mater., 2020, 3, 1875–1882.
- 36 M. Robertson, A. Griffin, A. G. Obando, A. Barbour, R. Davis and Z. Qiang, Precursor Design for Efficient Synthesis of Large-Pore, Sulfur-Doped Ordered Mesoporous Carbon through Direct Pyrolysis, *Mol. Syst. Des. Eng.*, 2023, **8**, 1156–1164.
- 37 M. Robertson, A. Guillen-Obando, A. Barbour, P. Smith, A. Griffin and Z. Qiang, Direct Synthesis of Ordered Mesoporous Materials from Thermoplastic Elastomers, *Nat. Commun.*, 2023, 14, 639.
- 38 M. Robertson, A. Barbour, A. Griffin, A. G. Obando, P. Smith and Z. Qiang, Sulfonation-Induced Cross-Linking and Nanostructural Evolution of a Thermoplastic Elastomer for Ordered Mesoporous Carbon Synthesis: A Mechanistic Study, *ACS Appl. Eng. Mater.*, 2023, 1, 2577–2588.

- 39 J. M. Younker, T. Saito, M. A. Hunt, A. K. Naskar and A. Beste, Pyrolysis Pathways of Sulfonated Polyethylene, Alternative Carbon Fiber Precursor, J. Am. Chem. Soc., 2013, 135, 6130-6141.
- 40 M. A. Hunt, T. Saito, R. H. Brown, A. S. Kumbhar and A. K. Naskar, Patterned Functional Carbon Fibers from Polyethylene, Adv. Mater., 2012, 24, 2386-2389.
- 41 B. E. Barton, J. Patton, E. Hukkanen, M. Behr, J. C. Lin, S. Beyer, Y. Zhang, L. Brehm, B. Haskins, B. Bell, B. Gerhart, A. Leugers and M. Bernius, The Chemical Transformation of Hydrocarbons to Carbon Using SO3 Sources, Carbon, 2015, 94, 465-471.
- 42 C. He, M. D. Guiver, F. Mighri and S. Kaliaguine, Surface Orientation of Hydrophilic Groups in Sulfonated Poly(Ether Ether Ketone) Membranes, I. Colloid Interface Sci., 2013, 409, 193-203.
- 43 K. Xia, Q. Gao, C. Wu, S. Song and M. Ruan, Activation, Characterization and Hydrogen Storage Properties of the Mesoporous Carbon CMK-3, Carbon, 2007, 45, 1989-1996.
- 44 Y. Yuan, Z. Chen, H. Yu, X. Zhang, T. Liu, M. Xia, R. Zheng, M. Shui and J. Shu, Heteroatom-Doped Carbon-Based Materials for Lithium and Sodium Ion Batteries, Energy Storage Mater., 2020, 32, 65-90.
- 45 Y. H. Abdelmoaty, T. D. Tessema, N. Norouzi, O. M. El-Kadri, J. B. M. G. Turner and H. M. El-Kaderi, Effective Approach for Increasing the Heteroatom Doping Levels of Porous Carbons for Superior CO2 Capture and Separation Performance, ACS Appl. Mater. Interfaces, 2017, 9, 35802-35810.
- 46 M. Zhong, S. Natesakhawat, J. P. Baltrus, D. Luebke, H. Nulwala, K. Matyjaszewski and T. Kowalewski, Copolymer-Templated Nitrogen-Enriched **Porous** Nanocarbons for CO2 Capture, Chem. Commun., 2012, 48, 11516-11518.
- 47 Z. Qiang, B. Gurkan, J. Ma, X. Liu, Y. Guo, M. Cakmak, K. A. Cavicchi and B. D. Vogt, Roll-to-Roll Fabrication of High Surface Area Mesoporous Carbon with Process-Tunable Pore Texture for Optimization of Adsorption Capacity of Bulky Organic Dyes, Microporous Mesoporous Mater., 2016, 227, 57-64.
- 48 S. Gadipelli, C. A. Howard, J. Guo, N. T. Skipper, H. Zhang, P. R. Shearing and D. J. L. Brett, Superior Multifunctional Activity of Nanoporous Carbons with Widely Tunable Porosity: Enhanced Storage Capacities for Carbon-Dioxide, Hydrogen, Water, and Electric Charge, Adv. Energy Mater., 2020, 10, 1903649.
- 49 D. Lozano-Castelló, J. M. Calo, D. Cazorla-Amorós and A. Linares-Solano, Carbon Activation with KOH as Explored by Temperature Programmed Techniques, and the Effects of Hydrogen, Carbon, 2007, 45, 2529-2536.
- 50 J. Jiang, H. Chen, Z. Wang, L. Bao, Y. Qiang, S. Guan and J. Chen, Nitrogen-Doped Hierarchical Porous Carbon Microsphere through KOH Activation for Supercapacitors, J. Colloid Interface Sci., 2015, 452, 54-61.
- 51 L. Zhao, L. Z. Fan, M. Q. Zhou, H. Guan, S. Qiao, M. Antonietti and M. M. Titirici, Nitrogen-Containing Hydrothermal Carbons with Superior Performance in Supercapacitors, Adv. Mater., 2010, 22, 5202-5206.

- 52 A. L. Cazetta, A. C. Martins, O. Pezoti, K. C. Bedin, K. K. Beltrame, T. Asefa and V. C. Almeida, Synthesis and Application of N-S-Doped Mesoporous Carbon Obtained from Nanocasting Method Using Bone Char as Heteroatom Precursor and Template, Chem. Eng. J., 2016, 300, 54-63.
- 53 M. Kopeć, R. Yuan, E. Gottlieb, C. M. R. Abreu, Y. Song, Z. Wang, J. F. J. Coelho, K. Matyjaszewski and Kowalewski, Polyacrylonitrile-b-Poly(Butyl Acrylate) Block Copolymers as Precursors to Mesoporous Nitrogenand Doped Carbons: **Synthesis** Nanostructure, Macromolecules, 2017, 50, 2759-2767.
- 54 Z. Qiang, Y. Xia, X. Xia and B. D. Vogt, Generalized Synthesis of a Family of Highly Heteroatom-Doped Ordered Mesoporous Carbons, Chem. Mater., 2017, 29, 10178-10186.
- 55 M. Robertson, A. GüIllen Obando, J. Emery and Z. Qiang, Multifunctional Carbon Fibers from Chemical Upcycling of Mask Waste, ACS Omega, 2022, 7, 12278-12287.
- 56 M. Robertson, A. G. Obando, B. Nunez, H. Chen and Z. Qiang, Upcycling Mask Waste to Carbon Capture Sorbents: A Combined Experimental and Computational Study, ACS Appl. Eng. Mater., 2022, 2023, 165-174.
- 57 H. Chen, Y. Xiong, T. Yu, P. Zhu, X. Yan, Z. Wang and S. Guan, Boron and Nitrogen Co-Doped Porous Carbon with a High Concentration of Boron and Its Superior Capacitive Behavior, Carbon, 2017, 113, 266-273.
- 58 L. Sui, Y. Wang, W. Ji, H. Kang, L. Dong and L. Yu, N-Doped Ordered Mesoporous Carbon/Graphene Composites with Supercapacitor Performances Fabricated by Evaporation Induced Self-Assembly, Int. J. Hydrogen Energy, 2017, 42, 29820-29829.
- 59 X. Wan, Y. Li, H. Xiao, Y. Pan and J. Liu, Hydrothermal Synthesis of Nitrogen-Doped Ordered Mesoporous Carbon via Lysine-Assisted Self-Assembly for Efficient CO 2 Capture, RSC Adv., 2020, 10, 2932-2941.
- 60 D. S. Yang, D. Bhattacharjya, S. Inamdar, J. Park and J. S. Yu, Phosphorus-Doped Ordered Mesoporous Carbons with Different Lengths as Efficient Metal-Free Electrocatalysts for Oxygen Reduction Reaction in Alkaline Media, J. Am. Chem. Soc., 2012, 134, 16127-16130.
- 61 Y. P. Zhu, Y. Liu, Y. P. Liu, T. Z. Ren, T. Chen and Z. Y. Yuan, Direct Synthesis of Phosphorus-Doped Mesoporous Carbon Materials for Efficient Electrocatalytic Oxygen Reduction, ChemCatChem, 2015, 7, 2903-2909.
- 62 G. Zhao, L. Shi, J. Xu, X. Yan and T. S. Zhao, Role of Phosphorus in Nitrogen, Phosphorus Dual-Doped Ordered Mesoporous Carbon Electrocatalyst for Oxygen Reduction Reaction in Alkaline Media, Int. J. Hydrogen Energy, 2018, 43, 1470-1478.
- 63 Y. Liu, L. Zhang, L. Cheng, W. Yang and Y. Xu, Effect of Deposition Temperature on Boron-Doped Carbon Coatings Deposited from a BCl3-C₃H₆-H₂ Mixture Using Low Pressure Chemical Vapor Deposition, Appl. Surf. Sci., 2009, 255, 8761-8768.
- 64 W. Cermignani, T. E. Paulson, C. Onneby and C. G. Pantano, Synthesis and Characterization of Boron-Doped Carbons, Carbon, 1995, 33, 367-374.

- 65 B. N. Yun, H. L. Du, J. Y. Hwang, H. G. Jung and Y. K. Sun, Improved Electrochemical Performance of Boron-Doped Carbon-Coated Lithium Titanate as an Anode Material for Sodium-Ion Batteries, J. Mater. Chem. A, 2017, 5, 2802–2810.
- 66 M. Ayiania, M. Smith, A. J. R. Hensley, L. Scudiero, J. S. McEwen and M. Garcia-Perez, Deconvoluting the XPS Spectra for Nitrogen-Doped Chars: An Analysis from First Principles, *Carbon*, 2020, **162**, 528–544.
- 67 P. Lazar, R. Mach and M. Otyepka, Spectroscopic Fingerprints of Graphitic, Pyrrolic, Pyridinic, and Chemisorbed Nitrogen in N-Doped Graphene, *J. Phys. Chem. C*, 2019, **123**, 10695–10702.
- 68 M. Sahoo, K. P. Sreena, B. P. Vinayan and S. Ramaprabhu, Green Synthesis of Boron Doped Graphene and Its Application as High Performance Anode Material in Li Ion Battery, *Mater. Res. Bull.*, 2015, 61, 383–390.
- 69 Z. Liu, Y. Du, P. Zhang, Z. Zhuang and D. Wang, Bringing Catalytic Order out of Chaos with Nitrogen-Doped Ordered Mesoporous Carbon, *Matter*, 2021, 4, 3161–3194.
- 70 H. Zhang, X. Li, D. Zhang, L. Zhang, M. Kapilashrami, T. Sun, P. A. Glans, J. Zhu, J. Zhong, Z. Hu, J. Guo and X. Sun, Comprehensive Electronic Structure Characterization of Pristine and Nitrogen/Phosphorus Doped Carbon Nanocages, *Carbon*, 2016, **103**, 480–487.
- 71 G. Hasegawa, T. Deguchi, K. Kanamori, Y. Kobayashi, H. Kageyama, T. Abe and K. Nakanishi, High-Level Doping of Nitrogen, Phosphorus, and Sulfur into Activated Carbon Monoliths and Their Electrochemical Capacitances, *Chem. Mater.*, 2015, 27, 4703–4712.
- 72 J. Wei, D. Zhou, Z. Sun, Y. Deng, Y. Xia and D. Zhao, A Controllable Synthesis of Rich Nitrogen-Doped Ordered Mesoporous Carbon for CO2 Capture and Supercapacitors, Adv. Funct. Mater., 2013, 23, 2322–2328.
- 73 M. Li and J. Xue, Integrated Synthesis of Nitrogen-Doped Mesoporous Carbon from Melamine Resins with Superior Performance in Supercapacitors, *J. Phys. Chem. C*, 2014, 118, 2507–2517.

- 74 M. Gao, L. Wang, Y. Yang, Y. Sun, X. Zhao and Y. Wan, Metal and Metal Oxide Supported on Ordered Mesoporous Carbon as Heterogeneous Catalysts, ACS Catal., 2023, 13, 4060–4090.
- 75 S. H. Joo, S. J. Choi, I. Oh, J. Kwak, Z. Liu, O. Terasaki and R. Ryoo, Ordered Nanoporous Arrays of Carbon Supporting High Dispersions of Platinum Nanoparticles, *Nature*, 2001, 412, 169–172.
- 76 W. Wang, H. Y. Wang, W. Wei, Z. G. Xiao and Y. Wan, Self-Assembling and Size-Selective Synthesis of Ni and NiO Nanoparticles Embedded in Ordered Mesoporous Carbon and Polymer Frameworks, *Chem. Eur. J.*, 2011, 17, 13461–13472.
- 77 P. Zhou, X. Wang, Z. Song, M. Wang, W. Huang, M. Yu, L. Wang and Q. Zhang, Multi-Dimensional Ordered Mesoporous Carbon/Silica@Ni Composite with Hierarchical Nanostructure for Strong and Broadband Microwave Absorption, *Carbon*, 2021, **176**, 209–218.
- 78 D. Dutta, A. Phukan and D. K. Dutta, Nanoporous Montmorillonite Clay Stabilized Copper Nanoparticles: Efficient and Reusable Catalyst for Oxidation of Alcohols, Mol. Catal., 2018, 451, 178–185.
- 79 H. Zheng, Y. He, Y. Zhu, L. Liu and X. Cui, Novel Procedure of CO2 Capture of the CaO Sorbent Activator on the Reaction of One-Part Alkali-Activated Slag, RSC Adv., 2021, 11, 12476– 12483.
- 80 R. Sun, P. Zhang, É. G. Bajnóczi, A. Neagu, C. W. Tai, I. Persson, M. Strømme and O. Cheung, Amorphous Calcium Carbonate Constructed from Nanoparticle Aggregates with Unprecedented Surface Area and Mesoporosity, ACS Appl. Mater. Interfaces, 2018, 10, 21556–21564.
- 81 T. L. Jin, X. Liu, Y. Q. Su, F. Pan, X. Han, H. Zhu, R. Wu and Y. Lyu, Mesoporous Carbon-Supported Ultrasmall Metal Nanoparticles *via* a Mechanochemical-Driven Redox Reaction: A "Two-in-One" Strategy, *Appl. Catal., B*, 2021, **294**, 120232.